JOURNAL OF APPLIED CRYSTALLOGRAPHY

ISSN 1600-5767

Received 3 January 2020
Accepted 12 March 2020

Edited by V. Holý, Charles University, Prague, Czech Republic and CEITEC at Masaryk University, Brno, Czech Republic

Keywords: crystal polishing; single-point diamond turning surface preparation; compressive stress; surface indentation; dislocations in indentation processes.

Compressive strain formation in surface-damaged crystals

Claudio Ferrari,[a]* Sara Beretta,[a] Enzo Rotunno,[b] Dusan Korytár[c] and Zdenko Zaprazny[c]

[a]1IMEM-CNR Institute, Parco Area delle Scienze 37/A, 43124 Parma, Italy, [b]NANO-CNR Institute, Via Campi 213/A, 41125 Modena, Italy, and [c]Institute of Electrical Engineering, Slovak Academy of Sciences, Dúbravská cesta 9, 841 04 Bratislava, Slovak Republic. *Correspondence e-mail: claudio.ferrari@imem.cnr.it

The mechanism of formation of residual strain in crystals with a damaged surface has been studied by transmission electron microscopy in GaAs wafers ground with sandpaper. The samples showed a dislocation network located near the sample surface penetrating to a depth of a few micrometres, comparable to the size of abrasive particles used for the treatment, and no other types of defects were observed. A simple model for the formation of a compressive strain induced by the dislocation network in the damaged layer is proposed, in satisfactory agreement with the measured strain. The strain is generated by the formation of dislocation half-loops at the crystal surface, having the same component of the Burgers vectors parallel to the surface of the crystal. This is equivalent to the insertion of extra half-planes from the crystal surface to the depth of the damaged zone. This model can be generalized for other crystal structures. An approximate calculation of the strain generated from the observed dislocation distribution in the sample agrees with the proposed model and permits the conclusion that this mechanism is in general sufficient to explain the observed compressive strain, without the need to consider other types of defects.

1. Introduction

The polishing of a crystal surface using abrasive media results in the formation of a compressive strain extending through a thickness comparable to the size of the abrasive particles. This strain in turn produces a permanent elastic bending of the whole crystal without external applied forces (Ferrari, Buffagni, Bonnini, & Korytar, 2013). On the basis of this method, permanently curved gallium arsenide, germanium and silicon plates of 2 mm in thickness can be obtained (Virgilli *et al.*, 2016; Liccardo *et al.*, 2014) with a very good reproducibility of the curvature value. This permanent curvature can be exploited for the preparation of lenses for gamma-ray astronomy (Buffagni *et al.*, 2014), nuclear medicine (Roa *et al.*, 2006), neutron-beam conditioning (Courtois *et al.*, 2006) and X-ray microscopy (Borbély & Kaysser-Pyzalla, 2013).

In the literature, empirical relationships can be found that correlate the sandpaper grit size, the crystal thickness and the induced curvature (Buffagni *et al.*, 2012):

(i) The radius of curvature R is proportional to the square of the sample thickness T.

(ii) The curvature and curvature shape depend on the orientation of the crystal surface and crystal symmetry: a spherical curvature in (001)-oriented Si or Ge crystals and an elliptical curvature in (100)-oriented GaAs or InP crystals.

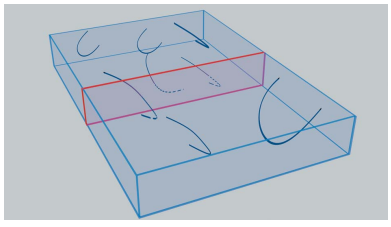

(iii) The curvature depends on the dimension of the abrasive particles or the grit size of the sandpaper used for the surface damage and on the pressure applied during the surface treatment.

A very similar effect, originally described by Twyman in 1905 (Twyman, 1905), is observed in plates made of amorphous materials. Experimental studies of polished glass or silicate reported that the surface compressive force increases with the average abrasive size with values of the surface tension of the order of several hundredths of a newton per metre, as reported for polished glass (Nikolova, 1985). The presence of surface compressive strain leads to a bowing of the plate with a radius of curvature R given by (Lambropoulos *et al.*, 1996; Rupp, 1987)

$$1/R = 8C/T^2, \tag{1}$$

in which T is the plate thickness. The constant C (∼nanometres) depends on the abrasive size and is often referred to as the Twyman constant. Accurate relationships are found between the induced local strain and the parameters of the polishing or grinding process, such as material, pressure, grit size and treatment time. However, a convincing physical explanation of the generation of the compressive strain in the damaged zone is essentially missing at present.

It has been proposed, for instance, that the amorphous layer produced by the relevant forces generated by the grinding particles on the crystal surface may lead to strain formation (Yan *et al.*, 2009; Chen & de Wolf, 2003), but it is not clear how a residual strain can be generated during the formation of the amorphous layer.

Another mechanism proposed for strain generation is based on the formation of cracks, that is the complete separation of crystalline planes (Haapalinna *et al.*, 2004; Holmström *et al.*, 2012), near the crystal surface after grinding or polishing. Again there is no physical explanation of how a crack can introduce compressive strain. Even if it is established that surface damage always produces compressive strain, cracks are not present in damaged surfaces in all cases.

Sun *et al.* (2017) proposed that grinding or polishing with abrasive particles could be considered as a multiple indentation process of the crystal surface. According to this idea, the formation of compressive strain is due to the indentation, but again the physical mechanism explaining the strain formation is not explained.

Strain formation in polished crystals is also relevant in the case of crystal surfaces prepared by nanomachining using single-point diamond turning (SPDT) (Korytár *et al.*, 2018). The minimization of subsurface damage generated by SPDT machining of Ge and Si crystal optics is of increasing importance with decreasing wavelength from infrared through visible, UV and X-rays. For shorter wavelengths – *e.g.* X-rays – shape precision, surface roughness, and subsurface damage and strains are very important technological parameters, which can negatively affect the performance of X-ray optical elements in metrological and imaging applications (Korytár *et al.*, 2013). For instance, the subsurface damage generated by SPDT machining of Si crystals was identified to consist mainly of microcracks, microcrystallites, dislocations, bundles of dislocations, local strains and a near-surface amorphous layer (Jiwang *et al.*, 2009).

To clarify the types of defects introduced and to understand the formation of the compressive strain in the damaged zone, we have analyzed by transmission electron microscopy (TEM) cross sections of gallium arsenide crystals in which the crystal surface was treated with sandpaper. X-ray measurements confirmed the formation of a compressive layer resulting in a convex curvature of the surface-damaged samples, as seen from the polished side. In the grinding process we expect the formation of the same types of defects as in mechanical polishing and in the SPDT nanomachining of crystals [see for instance Jergel *et al.* (2018)].

2. Experimental

2.1. Preparation of crystals

Slices of GaAs crystals grown by the liquid-encapsulated Czochralski method, of thickness in the range from 0.75 to 2 mm, were cut from ingots perpendicularly to the ⟨100⟩ growth direction. The initial saw damage was removed by chemical etching with a 1:1 HCl/HNO_3 solution.

The surface damage was achieved by means of a mechanical lapping process on one side of the planar samples using a Buehler Ecomec 4 polishing machine, which allowed us to produce different deformations by changing the setup: the grit of the sandpaper, the pressure applied on the samples and the duration of the treatment. The samples were mounted on a plate with paraffin, and then the plate was positioned upside down in the machine facing the sandpaper plate. The two components rotate independently on two different axes so the sample abrasion should be completely uniform across the entire surface of the sample plate.

The samples were lapped for 10 min with P400 sandpapers, corresponding to an approximate grain size of 35 µm, and applying constant force of approximately 5 N in samples 3 × 1 cm in size.

The prepared samples were characterized with a high-resolution X-ray X'Pert Pro PANalytical diffractometer by the method of measuring the change of Bragg condition as a function of position by translating the sample along the direction **x** parallel to the scattering plane. The crystal curvature is easily obtained by the formula

$$1/R = \Delta\theta_B/\Delta x, \tag{2}$$

in which $\Delta\theta_B$ is the shift of the Bragg peak position between two points separated by a distance Δx (Buffagni *et al.*, 2012). An experimental value of the radius of curvature R = 2.8 m was obtained in the sample considered in this study.

2.2. Transmission electron microscopy analysis

A preliminary report of this investigation has been published by Ferrari *et al.* (2018). Sample cross sections, parallel to (110) planes of the crystal, were mechanically polished down to *ca* 300 µm. The resulting foils were ion

sputtered with a Gatan DuoMill TM model 600, to reach electron transparency. The final sample thickness was estimated to be between 70 and 120 nm, as evaluated by the extinction length of an electron beam in the GaAs lamella. A final gentle ion-milling procedure was applied to the thin lamellae using a Gatan PIPS installation operated at 3 kV accelerating voltage and 7° incidence angle. The TEM microscope was a JEOL 2100 operating at 200 kV.

A typical cross-section scanning TEM image is reported in Fig. 1. No amorphous layers or cracks were seen in the TEM cross-section images obtained. The only visible defects in Fig. 1 are straight dislocation lines, visible as a whiter contrast. They are aligned along the traces of (111) planes perpendicular to the plane of the figure.

A series of TEM micrographs taken in a sample with the same treatment as described in Section 2.1 at higher magnification and recorded from neighbouring areas have been assembled in the panoramic image of Fig. 2, which illustrates the effect of the surface treatment and the distribution of dislocation lines in the first 3 μm below the surface. Straight dislocation segments starting from the surface to *ca* 0.3 μm in depth are observed. The two sets of dislocation lines have directions parallel to the traces of the $(1\bar{1}\bar{1})$ and $(1\bar{1}1)$ planes, perpendicular to the (110) surface of the TEM sample, as already observed in the scanning TEM image of Fig. 1. Looking carefully at the dislocation segments it appears that many dislocations cross the TEM sample, *i.e.* the dislocation lines are not parallel to the surface of the cross section.

The (001) processed surface is situated on the left-hand side of Fig. 2. The near-surface region shows a high defect density, mostly dislocations, that extends for a few hundreds of nanometres. Below this first layer the density of dislocations rapidly decreases, and the dislocations, which appear as straight dark lines, can be observed singly.

The area delimited by a dashed line was further analyzed in order to assess the nature of the observed defects. The area containing dislocations was imaged in the two-beam condition using three different scattering vectors: $\mathbf{g} = (00\bar{4})$, $\mathbf{g} = (1\bar{1}\bar{1})$ and $\mathbf{g} = (1\bar{1}1)$. The images presented in Fig. 3 are corrected for rotation between the imaging and the diffraction modes. Two families of parallel dislocations, marked with A and B in Fig. 3, are visible. By comparing the micrographs in Fig. 3, it is apparent that the habit planes of the two families of dislocations are $(1\bar{1}1)$ for family A and $(\bar{1}11)$ for family B.

The geometrical scheme of lattice planes and diffraction conditions is reported in Fig. 4.

By tilting the sample in such a way that the $(1\bar{1}\bar{1})$ and $(1\bar{1}1)$ reflections are excited, the B and A families of dislocations become respectively extinguished. It follows that, according to the $\mathbf{g}\cdot\mathbf{b}$ invisibility criterion, the Burgers vectors $\mathbf{b}$ of these dislocations are parallel to the {111} crystallographic planes.

Considering the A family of dislocations, from the orientation-imaging conditions it turns out that both the dislocation lines and their Burgers vectors are located in the $(1\bar{1}\bar{1})$ habit

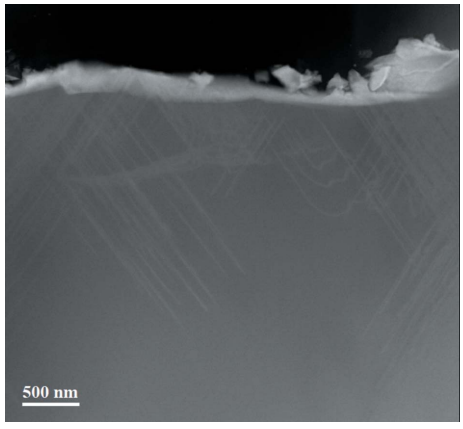

Figure 1
Cross-section (011)-projection of a scanning TEM image of the ground surface of a GaAs sample.

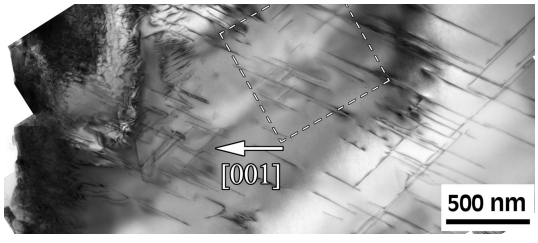

Figure 2
Cross-section (011)-projection TEM image of the ground surface of a GaAs sample, obtained by overlapping different TEM images. The dashed line corresponds to Fig. 3.

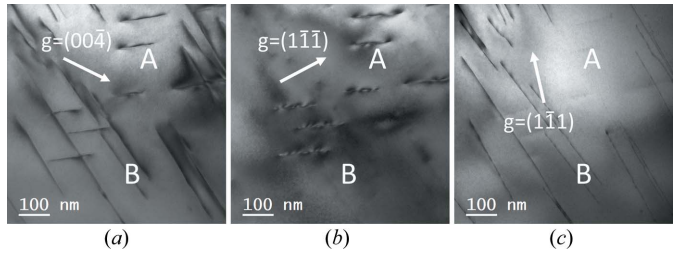

Figure 3
Series of TEM micrographs in the two-beam condition: left $\mathbf{g} = (00\bar{4})$; centre $\mathbf{g} = (1\bar{1}\bar{1})$; right $\mathbf{g} = (1\bar{1}1)$. Sample orientation close to the [110] zone axis. The two families of dislocations A and B are shown.

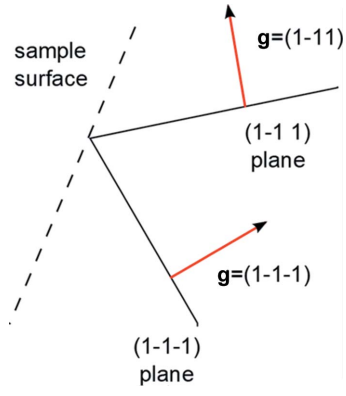

Figure 4
Crystallographic directions of Fig. 3.

plane. Knowing that in the cubic structure of GaAs with a slip system of the kind ⟨110⟩{111} the most common dislocations are perfect dislocations with Burgers vector $a/2\langle 110\rangle$, it follows that for the A-type dislocations the Burgers vectors may have one of the following six possible values: $a/2[110]$, $a/2[0\bar{1}1]$, $a/2[101]$ and their opposites, all of them contained in the $(\bar{1}11)$ A plane.

A similar analysis is valid for the B-type dislocations, for which the Burgers vectors lie in the $(1\bar{1}1)$ habit plane. The Burgers vector of B-type dislocations may have one of the following six possible values: $a/2[110]$, $a/2[\bar{1}01]$, $a/2[011]$ and their opposites, all of them contained in the $(1\bar{1}1)$ B plane.

The fact that the A and B dislocations are not extinguished simultaneously leads to the conclusion that the Burgers vector cannot be $a/2[110]$ or $a/2[\bar{1}10]$, parallel to the crystal surface (001). The Burgers vectors of the analyzed dislocations are one of the remaining four vectors: $a/2[0\bar{1}1]$, $a/2[101]$ and their opposites for the A planes and $a/2[\bar{1}01]$, $a/2[011]$ and their opposites for the B planes.

3. Model of compressive strain formation

To explain the compressive strain resulting from the surface grinding we propose that the process behaves as a multiple indentation in any direction along the surface. The indentation process in GaAs as in other face-centered cubic (f.c.c.) crystals results in the formation of rosettes made of dislocation loops gliding on (111) planes (Bradby *et al.*, 2001). A sketch of the proposed mechanism is shown in Fig. 5. As for GaAs and many other f.c.c. crystals, the easy glide system is of the type [110]{111}.

After the plastic deformation regime is initiated, the indentation is followed by the glide of dislocation half-loops along $(\bar{1}11)$ for the set of dislocations on the right of the tip and along $(1\bar{1}1)$ planes for the set on the left of the tip. In this drawing we neglect for the sake of simplicity the set of dislocations that are also formed and glide on (111) and $(1\bar{1}\bar{1})$ planes inclined with respect to the plane of the figure. In Fig. 5 the projections onto the plane of the figure of the Burgers vectors of the dislocations belonging to sets A and B are reported. The Burgers vector component is deduced by the shift of the crystal on one side of the glide plane with respect to that on the opposite part. To explain the subsidence of the part of the crystal just below the indentation tip, the dislocations gliding on $(\bar{1}11)$ and $(1\bar{1}1)$ planes must have opposite Burgers vector components perpendicular to the surface and equivalent components parallel to the surface. According to Fig. 5 (right) the Burgers vector generated by the indentation should be

$$\mathbf{b}_1 = \frac{a}{2}[\bar{1}0\bar{1}] \quad \text{or} \quad \mathbf{b}_2 = \frac{a}{2}[01\bar{1}] \tag{3}$$

for the $(\bar{1}11)$ glide plane (A) and

$$\mathbf{b}_3 = \frac{a}{2}[\bar{1}01] \quad \text{or} \quad \mathbf{b}_4 = \frac{a}{2}[011] \tag{4}$$

for the $(1\bar{1}1)$ (B) plane.

These Burgers vectors belong to the possible set of Burgers vectors as deduced by extinction-contrast TEM images, thus confirming the validity of the model. According to this model several dislocation loops are generated at the surface and penetrate into the crystal to different depths, as sketched in Fig. 6.

Considering the strain induced in the crystals by the presence of dislocation loops produced by indentation, we can consider that the average strain induced by the trailing segments vanishes. However, owing to the non-random distribution of Burgers vectors, the dislocation lines near the bottom of the loops give a net contribution to the strain. This is similar to the case of a partially relaxed epitaxial layer grown on a substrate, where the misfit dislocations have the same Burgers vector components parallel to the interface to accommodate the lattice mismatch (Ferrari *et al.*, 2018).

As illustrated in Fig. 7, we can estimate that the strain is equivalent to that given by a linear density ρ of misfit dislocations, where the linear density is given by the area density

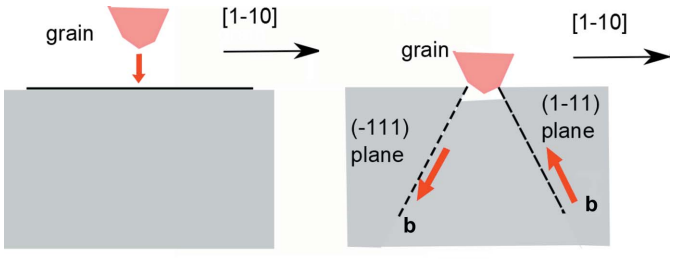

Figure 5
(Left) Movement of the tip of a grain of the grinding paper in a direction perpendicular to the (001) surface of the crystal. (Right) The shift of part of the crystal below the original surface due to indentation.

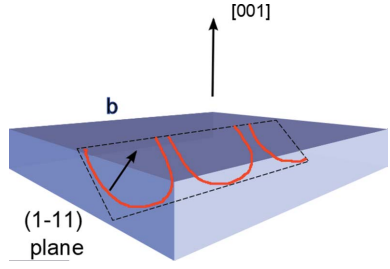

Figure 6
Glide of dislocation half-loops generated by the indentation of the grains of the sandpaper.

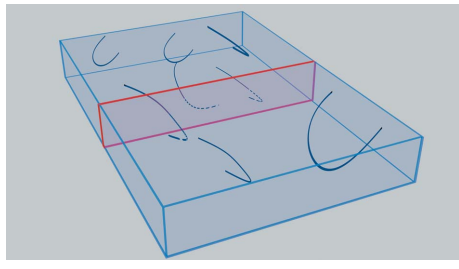

Figure 7
Apparent linear density of dislocations as obtained for a section S of the sample.

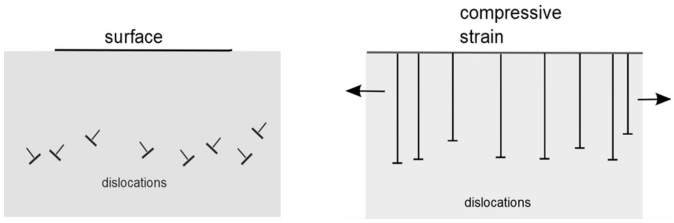

Figure 8
Burgers vectors of the dislocations generated by surface damage. On the left, randomly distributed Burgers vectors are shown with a common component parallel to the surface. On the right, the parallel component of the dislocation line corresponds to the insertion of an extra half-plane from the surface of the crystal, resulting in a compressive strain of the dislocated zone.

ρ_A of dislocation loops and the average length $\langle l \rangle$ crossed by a section S:

$$\rho = \rho_A \langle l \rangle. \tag{5}$$

The linear density is equivalent to the number of dislocation loops crossed by the section S. Assuming the crystal thickness $t \ll$ the loop dimension, from Fig. 1 we can evaluate a dislocation density $\rho = 15 \pm 3\ \mu^{-1}$.

The situation is depicted in Fig. 8, in which a representation of the Burgers vector with the corresponding extra half-planes is drawn.

4. Compressive strain evaluation

According to Fig. 5 (right) the Burgers vectors of the dislocations generated by indentation must have the same component parallel to the (001) surface and opposite components perpendicular to the (001) surface: from Fig. 5 (right) possible Burgers vectors of the dislocation loops are $a/2[\bar{1}01]$ and $a/2[011]$ for the $(\bar{1}11)$ plane on the left side of the tip and $a/2[\bar{1}0\bar{1}]$ and $a/2[01\bar{1}]$ for the $(1\bar{1}1)$ plane on the right. Each loop contributes with a Burgers vector edge component $b^{//} = a/2$ along the $[1\bar{1}0]$ direction, whereas the average of the normal component $b^{\perp}$ is zero.

Looking at the loop segments and considering the Burgers vector edge component $b^{\perp} = a/2$ parallel to the (001) surface of the sample, where $a = 5.6535$ Å is the GaAs lattice parameter, and a linear dislocation density $\rho = 15 \pm 3\ \mu m^{-1}$, the network of dislocations appears as a series of extra half-planes with a strain f of the damaged layer (difference between the lattice parameter of the compressed layer and the lattice parameter of the free layer) with respect to the unperturbed deep crystal:

$$\begin{aligned} f &= \rho a/2 = 15 \times 10^3\ \text{mm}^{-1} \times 2.82 \times 10^{-6}\ \text{mm} \\ &= 4.2 \times 10^{-3} \pm 0.8 \times 10^{-3}. \end{aligned} \tag{6}$$

The Stoney equation applied to an isotropic medium relates the stress σ_f of a film of thickness t_f to the curvature R of the substrates of thickness T (Nikolova, 1985):

$$\sigma_f t_f = \frac{E_s T^2}{6(1-\nu_s)}, \tag{7}$$

in which E_s and ν_s are the Young modulus and the Poisson ratio of the substrate. For a biaxial strain in a (001)-oriented cubic crystal the strain f and the stress σ_f are related by

$$\sigma_f = (c_{11} + c_{12} - 2c_{12}^2/c_{11})f, \tag{8}$$

in terms of the elastic constants c_{11} and c_{12}. For a (001)-oriented cubic crystal equation (8) can be rewritten in terms of the Poisson ratio $\nu = c_{12}/(c_{11} + c_{12})$ and Young modulus $E = (c_{11}^2 + c_{11}c_{12} - 2c_{12}^2)/(c_{11} + c_{12})$ as

$$\sigma_f = \frac{E_f}{1-\nu_f} f. \tag{9}$$

We then obtain the simplified expression independent of the elastic constants:

$$ft = T^2/(6R). \tag{10}$$

Assuming a strain value $f = 4.2 \times 10^{-3} \pm 0.8 \times 10^{-3}$, a strained layer thickness $t \simeq 2\ \mu m$ and a crystal thickness $T = 0.36$ mm, we obtain the curvature radius $R = 2.6 \pm 0.5$ m, in satisfactory agreement with the observed curvature, thus demonstrating that the mechanism based on dislocation propagation is sufficient to justify the measured stress.

The stress value σ_f can be calculated from the corresponding stress–strain relationship by assuming a biaxial stress $\sigma_{xx} = \sigma_{yy}$, $\sigma_{zz} = 0$ (Ferrari, Buffagni & Rossi, 2013), in which $\sigma_{xx} = \sigma_{yy}$ are the stress components parallel to the crystal surface and σ_{zz} is the stress component perpendicular to the crystal surface. $c_{12} = 5.34 \times 10^{11}$ dyn cm^{-2} and $c_{11} = 11.9 \times 10^{11}$ dyn cm^{-2} are the elastic constants of the GaAs crystal (http://www.ioffe.ru/SVA/NSM/Semicond/GaAs/mechanic.html#Elastic; 1 dyn = 10^{-5} N). So we obtain

$$\sigma_f = 12.4 \times 10^{10} \times 4.2 \times 10^{-3}\ \text{N m}^{-2} = 5.2 \times 10^8\ \text{N m}^{-2}, \tag{11}$$

comparable to values reported previously (Buffagni *et al.*, 2012; Lambropoulos *et al.*, 1996; Nikolova, 1985).

5. Conclusions

A GaAs crystal with the (001) surface ground by sandpaper has been characterized by transmission electron microscopy in cross-section geometry. After the surface damage the TEM images showed a surface roughness comparable to the grit of the sandpaper and a network of straight dislocation segments originating from the surface and lying on (111) and $(1\bar{1}\bar{1})$ planes, inclined to the (001) surface of the crystal and extended to a depth of up to 3 µm. No other types of defects, such as cracks or inclusions or amorphous phases, were detected. The Burgers vectors of the generated dislocations have been established by following the extinction-contrast rules.

A simple model is proposed for the formation of compressive strain in the damaged layer, giving a satisfactory agreement with the measured sample curvature and strain. The model is based on the glide of dislocations and explains the difference in the observed curvature in samples with different orientations as due to the different dislocation glide

velocities. This may also explain the elliptical curvature in polar samples, such as GaAs, due to the different dislocation velocities on (111) glide planes.

According to this simple model, the strain is generated by the formation of dislocation loops having the same component of the Burgers vector parallel to the surface of the crystal, whereas the average of the perpendicular components is zero. This is equivalent to the insertion of extra half-planes introduced from the crystal surface to a depth t, the thickness of the damage zone. This model can be generalized for other crystal structures.

An approximate calculation of the strain generated by the observed dislocation density in the sample examined permits us to conclude that this mechanism is in general sufficient to explain the strain observed, without considering other types of defects such as cracks or amorphous phases.

We also conclude that the absence of dislocations near the polished surface is a good indication of the absence of residual strain, which is very important in crystals prepared by the SPDT technique: limiting the formation of dislocations reduces the amount of residual strain induced by the crystal processing.

Funding information

This work is supported by the INAF-ASI project No. 2017-14-H.O. Technological Readiness Level Increase for Laue Lenses (TRILL), projects of the Research and Development Center for Advanced X-ray Technologies (ITMS code 26220220170) of the Slovak Research and Development Agency (APVV-14-0745), and the Scientific Grant Agency of the Ministry of Education of the Slovak Republic and the Slovak Academy of Sciences (VEGA-2/0092/18)

References

Borbély, A. & Kaysser-Pyzalla, A. R. (2013). *J. Appl. Cryst.* **46**, 295–296.
Bradby, J. E., Williams, J. S., Wong-Leung, J., Swain, M. V. & Munroe, P. (2001). *Appl. Phys. Lett.* **78**, 3235–3237.
Buffagni, E., Ferrari, C., Bonnini, E. & Zappettini, A. (2014). *Opt. Eng.* **53**, 047104.
Buffagni, E., Ferrari, C., Rossi, F., Marchini, L. & Zappettini, A. (2012). *Opt. Eng.* **51**, 056501.
Chen, J. & de Wolf, I. (2003). *Sci. Tech.* **18**, 261.
Courtois, P., Bigault, T., Andersen, K. H., Baudin-Cavallo, J., Ben Saïdane, K., Berneron, M., El-Aazzouzzi, A., Gorny, D., Graf, W., Guiblain, T., Hehn, R., Hetzler, E., Menthonnex, C., Mestrallet, B. & Dewhurst, C. (2006). *Physica B*, **385–386**, 1271–1273.
Ferrari, C., Buffagni, E., Bonnini, E. & Korytar, D. (2013). *J. Appl. Cryst.* **46**, 1576–1581.
Ferrari, C., Buffagni, E. & Rossi, F. (2013). *Characterization of Semiconductor Heterostructures and Nanostructures*, 2nd ed., edited by C. Lamberti & G. Agostini, ch. 3, p. 77. Amsterdam: Elsevier.
Ferrari, C., Ghica, C. & Rotunno, E. (2018). *Crystals*, **8**, 67.
Haapalinna, A., Nevas, S. & Pähler, D. (2004). *Mater. Sci. Eng. B*, **107**, 321–331.
Holmström, E., Kotakoski, J., Lechner, L., Kaiser, U. & Nordlund, K. (2012). *AIP Adv.* **2**, 012186.
Jergel, M., Halahovets, Y., Maťko, I., Korytár, D., Zápražný, Z., Hagara, J., Nádaždy, P., Šiffalovič, P., Kečkéš, J. & Majková, E. (2018). *Int. J. Adv. Manuf. Technol.* **96**, 3603–3617.
Jiwang, Y., Tooru, A., Hirofumi, H. & Tsunemoto, K. (2009). *Precis. Eng.* **33**, 378–386.
Korytár, D., Vagovič, P., Ferrari, C., Šiffalovič, P., Jergel, M., Dobročka, E., Zápražný, Z., Áč, V. & Mikulik, P. (2013). *Proc. SPIE*, **8848**, 8848U.
Korytár, D., Zápražný, Ferrari, C., Frigeri, C., Jergel, M., Maťko, I. & Kečkeš, J. (2018). *Appl. Opt.* **57**, 1940–1943.
Lambropoulos, J. C., Xu, S., Fang, T. & Golini, D. (1996). *Appl. Opt.* **35**, 5704–5713.
Liccardo, V., Virgilli, E., Frontera, F., Valsan, V., Buffagni, E., Ferrari, C., Bonnini, E., Zappettini, A., Guidi, V., Bellucci, V. & Camattari, R. (2014). *Exp. Astron.* **38**, 401–416.
Nikolova, E. G. (1985). *J. Mater. Sci.* **20**, 1–8.
Roa, D. E., Smither, R. K., Zhang, X., Nie, K., Shieh, Y. Y., Ramsinghani, N. S., Milne, N., Kuo, J. V., Redpath, J. L., Al-Ghazi, M. S. A. L. & Caligiuri, P. (2006). *Exp. Astron.* **20**, 229–239.
Rupp, W. J. (1987). *Optical Fabrication and Testing Workshop*, pp. 25–30. Washington, DC: Optical Society of America.
Sun, K., Shi, J. & Ma, L. (2017). *Crystals*, **7**, 240.
Twyman, F. (1905). *Proceedings of the Optical Convention*, p. 78. London: Northgate & Williams.
Virgilli, E., Frontera, F., Rosati, P., Bonnini, E., Buffagni, E., Ferrari, C., Stephen, J. B., Caroli, E., Auricchio, N., Basili, A. & Silvestri, S. (2016). *Exp. Astron.* **41**, 307–326.
Yan, J., Asami, T., Harada, H. & Kuriyagawa, T. (2009). *Precis. Eng.* **33**, 378–386.